Chapter 4

"*p*-Thiocresol functionalized Cesium Lead Bromide ($PTC@CsPbBr_3$): As a fluorometric sensing probe for the detection of Cholesterol"

Highlights: This chapter discloses a fluorescence-based sensing method with *p*-Thiocresol functionalized Cesium Lead Bromide ($PTC@CsPbBr_3$) for detection of cholesterol. The main highlights of the chapter are its synthetic method, its selectivity in presence of biologically active molecules and extension towards real samples.

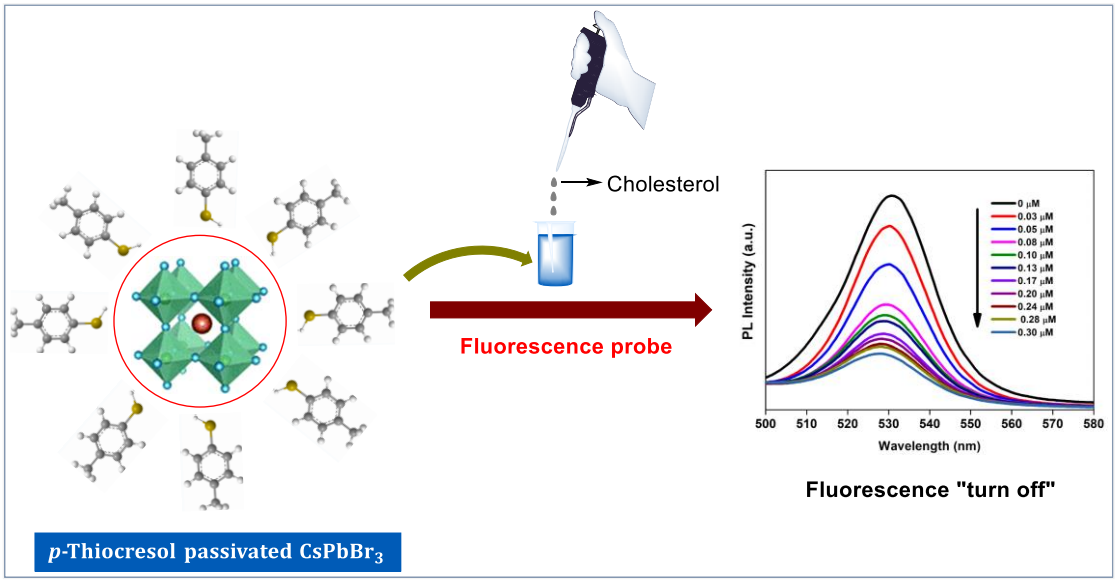

4.1 Introduction

Cholesterol belongs to an essential class of lipids in the human body (Figure 4.1). It is a waxy, fat-like substance and can be found in the brain, nerve cells, liver, skin, etc. It plays a very important role in the construction of the hormonal system and acts as a synthesis precursor of many vitamins, steroid hormones, and bile ducts [1]. However, cholesterol is also the reason for many diseases when its limit is not under optimal level. In human blood serum, the total concentration of cholesterol should be in the range of 2.86-5.98 mM. For instance, when cholesterol level goes below this level and it causes several diseases such as anemia, hemorrhage, hypothyroidism, and even cancer, etc [2,3]. On the other hand, a higher cholesterol level than the optimal range is harmful to the human body, and diseases like arteriosclerosis, nephritic syndrome, heart diseases, myocardium infection, and lipid metabolism can be happened [4]. Therefore, it is necessary to maintain an accurate level of cholesterol in our blood serum to get rid of cholesterol-related diseases.

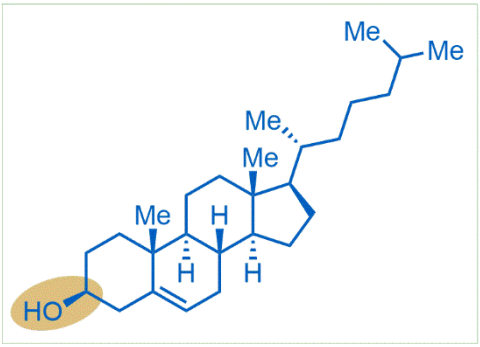

Figure 4.1 Molecular structure of cholesterol

In that context, many spectroscopic technologies have been developed over different periods to detect cholesterol in serum. The common detection techniques used to detect cholesterols are fluorometric [5], electrochemical [6], enzymatic methods [7], liquid-phase chromatographic [8], etc. Notably, all these methods have their own advantages and some disadvantages while using those detection processes. Most of those techniques required expensive instruments, and they need a complicated operating process with low selectivity and sensitivity. Recently, fluorescence chemo-sensors have gained much attention because of the advantages of simple operations, low-cost, rapid detection time, and excellent luminescent properties [9-14]. Till now, various fluorescence sensors like metal-organic frameworks (MOF) [15,16], polymers [16],

quantum dots [17], and carbon dots [18] have been successfully applied to detect cholesterol at an accurate level.

In the concurrent research period, perovskites (ABX_3) have been explored in various applications such as emitting diodes (LED), solar cells, sensors, photodetectors, photocatalysts, etc. due to their outstanding optoelectronic properties [19-27]. Recently $CsPbBr_3$ perovskites have been witnessed to construct many photoluminescent (PL), chemiluminescent, electroluminescent, and colorimetric sensor probes for detecting metal ions, pesticides, gas molecules, humidity, etc. Among the various techniques, the fluorescence detection method is one of the most applied techniques where the fluorophore can detect the analyte with a lower detection limit. However, the degradation in humid conditions is a major drawback in the case of halide-based perovskites. In presence of humidity, the $CsPbBr_3$ degraded into $PbBr_2$ and CsBr and become non-functional to act as sensors. Many passivating and encapsulation processes have been developed to stabilize the perovskite moiety. For example, polymers, MOF [28], COF [29], and TiO_2 [30] have been utilized as passivating ligands for $CsPbBr_3$ and make the material substantially stable. Wang et al., developed 3-aminopropyltriethoxysilane (APTES) passivated $CsPbBr_3$ as a fluorescence sensor to detect tetracycline in an ethanol medium [17]. Later, Shu et al., first synthesized $CsPbBr_3$ encapsulated in silica and methoxy polyethylene glycol to make a humid-stable fluorescence sensor for the detection of the analyte Hg^{2+} and glutathione [31]. Xue and co-workers reported passivated $CsPbBr_3$ gold and SiO_2 and represented the designed sensor as a ratio-metric fluorescence sensor probe towards the copper ions [32].

With this above discussion, this chapter highlighted the synthesis of stable passivated $CsPbBr_3$, perovskite nanocrystals by using oleic acid (OA) and *p*-thiocresol as a passivating ligand to make perovskite nanocrystals (PNCs) to increase the stability. The discussion about the luminescence stability of the ligand passivated $CsPbBr_3$ towards photo, temperature, and aqueous stabilities of PNCs compared to the pristine one is mentioned. Later, the application of the passivated sensor probe as a fluorescence-sensing probe for cholesterol detection is studied. To validate the sensing performance in real sample assay, the sensing method developed in this work is further studied in human blood serum to prove its practical ability to detect cholesterol in biomedical applications.

4.2 Experimental

4.2.1 Materials

All chemicals were used without purification. Cesium Bromide (CsBr) (99.9%, Alfa Aesar), Lead Bromide ($PbBr_2$) (99.9%, TCI), Dimethylformamide (DMF) (99%, Alfa Aesar), *p*-Thiocresol (99%, Sigma-Aldrich), Toluene (99%, Alfa Aesar), Oleic Acid (OA) (99.9%, TCI), Cholesterol (Sigma-Aldrich), Urea (Sisco Research Laboratories), Glycine (Alfa Aesar), Fructose (Alfa Aesar), *L*-Cysteine (Alfa-Aesar), Rhodamine Blue (Sigma-Aldrich), Ethanol (99%, Alfa Aesar), Ascorbic Acid (Alfa Aesar), Uracil (Alfa Aesar), Alanine (Sigma-Aldrich), Glucose (Sigma-Aldrich), Adenine (Alfa Aesar), Cystine (Alfa Aldrich), NaCl (SRL), KCl (SRL) are commercially available.

4.2.2 Synthesis of *p*-thiocresol passivated $CsPbBr_3$

The PTC@$CsPbBr_3$ PNCs were synthesized using this procedure: dissolving 0.4 mmol of CsBr, and 0.4 mmol of $PbBr_2$, 1 mL of oleic acid, 0.1 mmol of *p*-thiocresol in 10 mL DMF to form a clear precursor solution [27]. Later, 1 mL of the above solution was dropped to 10 mL toluene with vigorous stirring. The obtained product was centrifuged, washed with toluene several times, and dried in a vacuum oven at 80 ℃ to obtain pure and dried material.

4.2.3 Structural Characterization

The FT-IR spectra of the samples were performed using a Nicolet Impact-410 IR spectrometer (USA) in the KBr medium at room temperature in the range of 4000–400 cm^{-1}. XRD was measured with Bruker D8 advanced eco P-XRD system. The surface morphologies of $CsPbBr_3$ metal halide perovskites (MHPs) were analyzed by using Gemini 500 FE-SEM instrument and energy dispersive compositional mappings were recorded by using SEM (JEOL-JSM-6390LV). The High-resolution Transmission Electron Microscope (HR-TEM) images were captured using (Model: JEM-2100, JEOL, USA). The chemical compositions were analyzed by X-ray photoelectron spectroscopy (XPS, Perkin Elmer model 1257). A Shimadzu UV-2550 spectrophotometer was used to record the electronic absorption spectra of the samples in the wavelength range of 200-800 nm. The fluorescence emission spectra were recorded using a Hitachi F-2700 fluorescence spectrophotometer at room temperature. The decay of fluorescence spectra was measured using (Horiba Scientific, instrument) model.

4.2.4 Fluorescence measurements

The quantum yield of the PTC@$CsPbBr_3$ perovskite crystals was calculated by considering Rhodamine Blue as a reference (Quantum Yield = 97 % in ethanol). The measurements were carried out using the equations as follows [33,34].

$$\Phi_{fx} = \frac{\eta_x^2}{\eta_{Rhodamine\ Blue}^2} \cdot \frac{A_{Rhodamine\ Blue}}{A_x} \cdot \frac{F_x}{F_{Rhodamine\ Blue}} \cdot \Phi_{fRhodamine\ Blue}$$

In the above equation, η is the refractivity (η = 1.36 for ethanol, and η= 1.49 for toluene), A is the absorbance which is lower than 0.01 to avoid internal filter effects [34] and F is the integral absorption area in the luminescence spectra.

4.2.5 Methods for stability experiments

The stability experiments were carried out using a dispersion of 0.1 mmol of $CsPbBr_3$ (0.057 g) in 10 mL toluene. The suspension was further sonicated for 30 min to get a homogeneous mixture. 3 mL of the above perovskite aliquot was taken in a cuvette and their respective luminescence peak was recorded under the excitation wavelength of 380 nm. The experiments were carried out in a humid condition of 80%. The photostability test was done by taking 3 mL of the above suspension under the illumination of a 365 nm UV lamp for a period of 8 hours. The thermal stability of the passivated PNCs was measured while increasing the temperature of the suspension up to 110 ℃.

4.2.6 Fluorescence detection of cholesterol using PTC@$CsPbBr_3$ sensor probe

To investigate the sensing experiments, a homogeneous dispersion of passivated PNCs was made having a concentration of (0.57 g/100 mL) under sonication for 30 min. After, 3 mL of this suspension was placed in a quartz cuvette and to that various concentration of cholesterol was added. The respective luminescence measurements were carried out under the excitation wavelength was 380 nm.

4.2.7 Detection of cholesterol in real samples

The practical applicability of the sensor probe was studied in human blood serum samples with the target analyte. The blood serum samples were collected from the Health Centre of Tezpur University. Then the samples were further diluted 100 times. Then, the samples were mixed with different concentrations of cholesterol for the respective fluorescence measurements under the excitation wavelengths of 380 nm. The recovery rate of the blood samples was calculated.

4.3 Results and Discussion

4.3.1 Structural Analysis

4.3.1.1 FT-IR spectra

To analyze the functional groups, the FT-IR spectra were recorded (Figure 4.2). The absorption band at 2915 and 2848 cm^{-1} is attributed to the asymmetric and symmetric stretching modes of C-H vibration [35,36]. The absorption band at 3437 cm^{-1} is corresponding to the presence of absorbed H_2O molecules [36]. The peak appeared at 1396 cm^{-1} is due to the bending vibrations of the C-H bond. The successful passivation of *p*-thiocresol was also proved by the absorption peak appearing at 1394 and 2400 cm^{-1} due to the stretching mode of vibration of the C-S and S-H bond, respectively [34, 37].

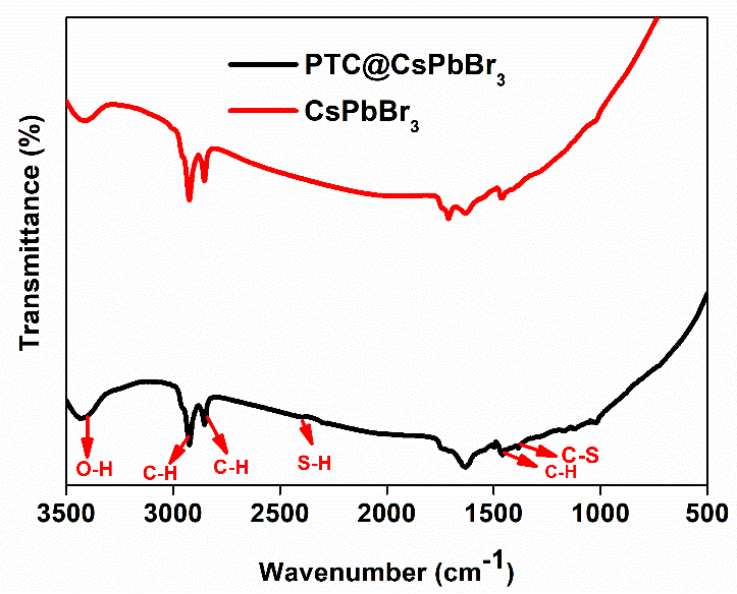

Figure 4.2 FT-IR spectra of PTC@$CsPbBr_3$ & $CsPbBr_3$

4.3.1.2 PXRD analysis

To study the effect of passivation upon crystal phases, P-XRD analysis of the prepared materials was recorded. The diffraction peaks (110), (112), and (220) indexed at 15.19, 21.48, and 30.58 were observed (Figure 4.3). From this data, it was confirmed that the synthesized perovskites have standard orthorhombic phase [38].

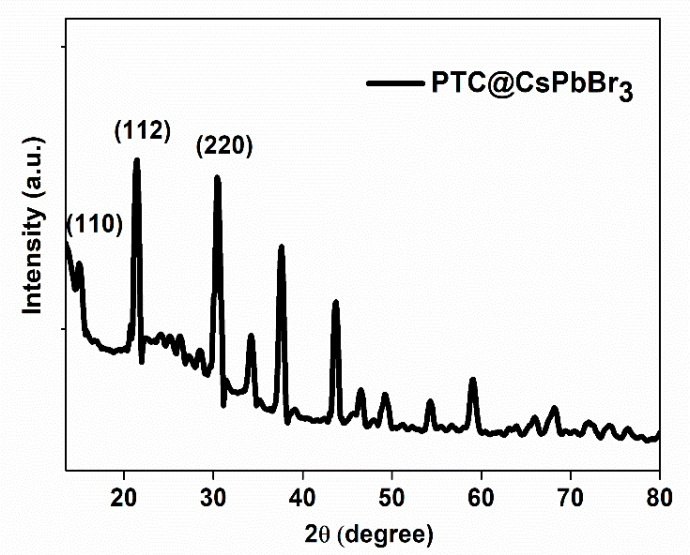

Figure 4.3 P-XRD spectrum of PTC@$CsPbBr_3$ crystal

4.3.1.3 Optical analysis

The optical analysis in this work employed that the synthesized passivated perovskite exhibits a characteristic broad absorbance maximum till 520 nm and a sharp emission peak at 530 nm with full-width half maxima (FWHM) (26 nm) upon excitation at 380 nm (Figure 4.4). The inset image displayed a bright green color of PTC@$CsPbBr_3$ dispersion under the illumination of UV light at 365 nm. The calculated quantum yield of PTC@$CsPbBr_3$ was found as 55.62% (Table 4.1). Moreover, the UV-Vis absorbance of *p*-thiocresol passivated $CsPbBr_3$ was found more in comparison to pristine $CsPbBr_3$ (Figure 4.5).

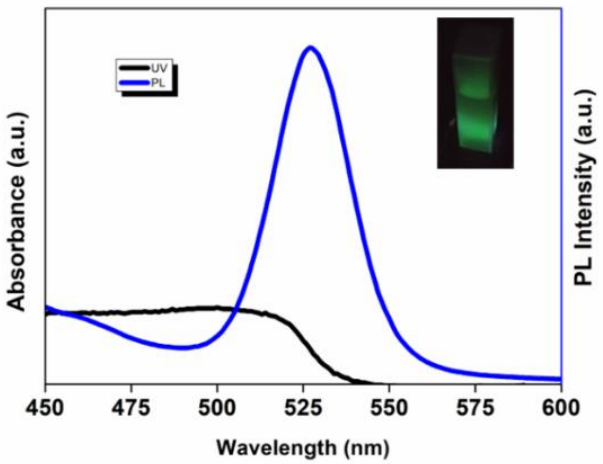

Figure 4.4 Luminescence and absorbance spectra of PTC@$CsPbBr_3$ dispersion with the inset images display the color of the passivated perovskite nanocrystals under the irradiation of 365 nm UV-lamp

Furthermore, the lifetime of the pristine perovskite and the passivated perovskites were calculated (Figure 4.6). The decay graphs were well-fitted in a bi-exponential decay. The average lifetime value of $CsPbBr_3$ showed increment from 1.16 ns to 5.91 ns upon PTC passivation. The increased lifetime values in PTC@$CsPbBr_3$ indicate the enhancement of stability in the excited state after passivation with *p*-thiocresol.

Table 4.1 Summary of relative photoluminescence quantum yield of PTC@$CsPbBr_3$ & $CsPbBr_3$

Perovskite Sample	PLQY (%)
PTC@$CsPbBr_3$	55.62
$CsPbBr_3$	18.70

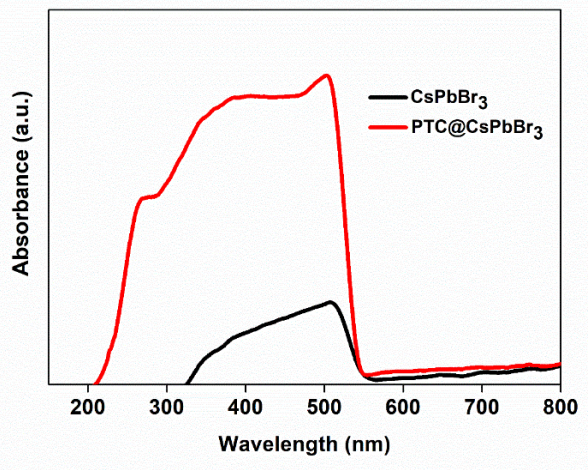

Figure 4.5 UV-Vis absorption spectra of $CsPbBr_3$ and PTC@$CsPbBr_3$

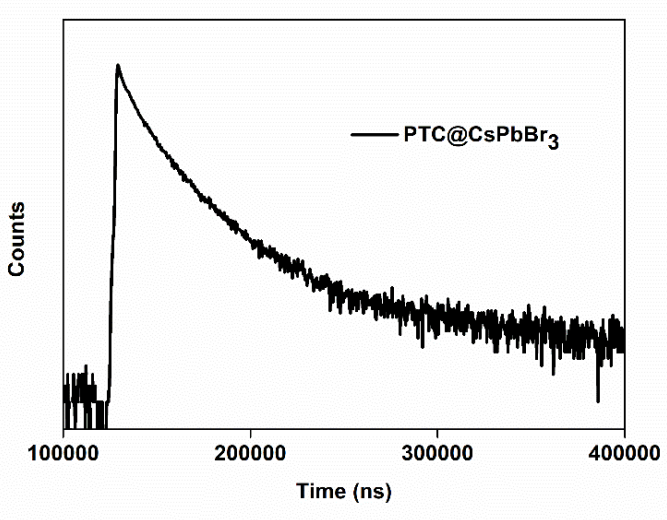

Figure 4.6 Time-resolved Photo-luminescence decay graph of PTC@$CsPbBr_3$

4.3.1.4 Energy dispersive X-ray (EDX) analysis

The distribution of different elements was confirmed by EDX analysis (Figure 4.7). The presence of the elements such as Cs, Pb, Br, C, and S were found with a close approximation to their atomic percentage of 13.5:10.83:37.06:37.31:1.3. The elemental mapping images of the synthesized perovskite were described the homogeneous distribution of all the elements in the crystal lattice (Figure 4.8).

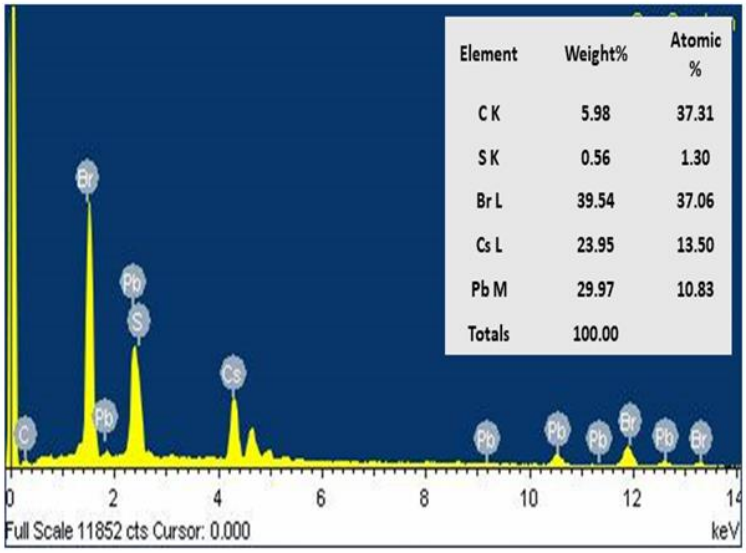

Figure 4.7 EDX spectra of PTC@$CsPbBr_3$ with the inset image show the elemental ratios

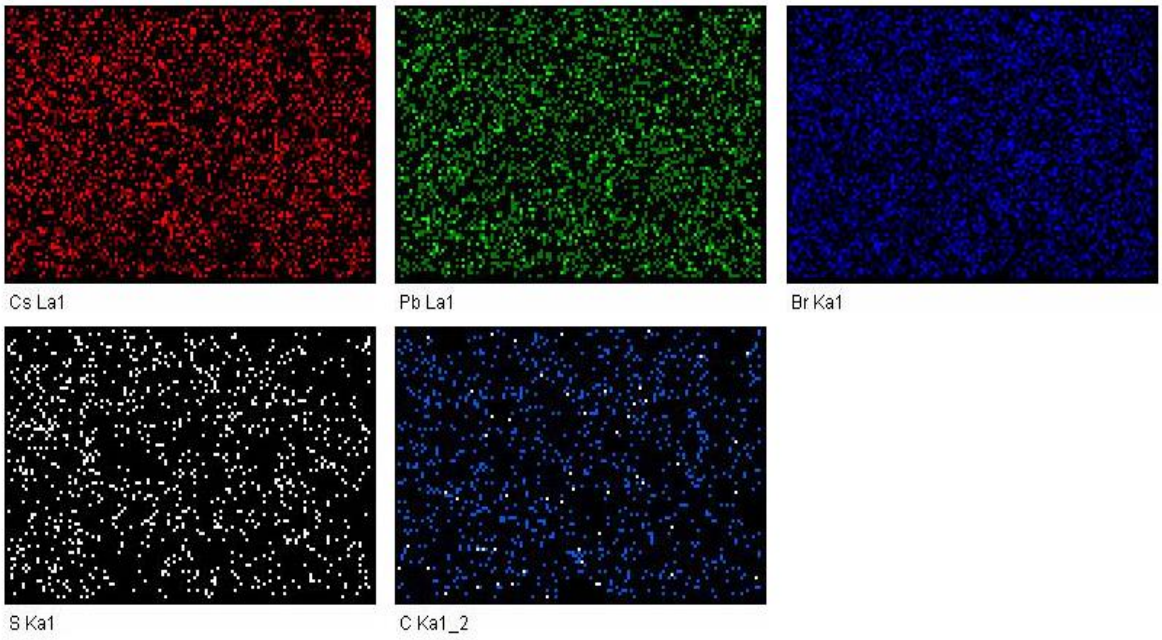

Figure 4.8 Elemental mapping images for elements such as Cs, Pb, Br, C, and S

4.3.1.5 X-ray Photoelectron spectroscopy (XPS) analysis

The high-resolution X-ray Photoelectron spectroscopy (XPS) was performed, and the analysis revealed the detection of Cs, Pb, Br, C, and S elements in the PTC@$CsPbBr_3$ nanocrystal lattice. This study again proved about the successful passivation of *p*-thiocresol group into the perovskite crystal lattice. The binding energies for Cs $3d_{3/2}$ and Cs $3d_{5/2}$ appeared at 738 eV and 724 eV, respectively (Figure 4.9a). Similarly, the binding energies observed at 143.2 eV and 138.2 eV are observed due to Pb $4f_{5/2}$ and Pb $4f_{3/2}$, respectively (Figure 4.9b). With the binding energies 69.1 eV and 68.2 eV, the Br 3d peak is deconvoluted into two sub-peaks that are Br $3d_{5/2}$ and Br $3d_{3/2}$ (Figure 4.9c). Also, the peak for C 1s appeared at 284.6 eV, and the peak appeared at 170 eV and 164 eV were observed due to S 2p (Figure 4.9d-e) [39]. The elemental ratios of the elements found from XPS data are outlined. The XPS data confirmed the successful passivation of *p*-thiocresol into the perovskite crystal lattice structure.

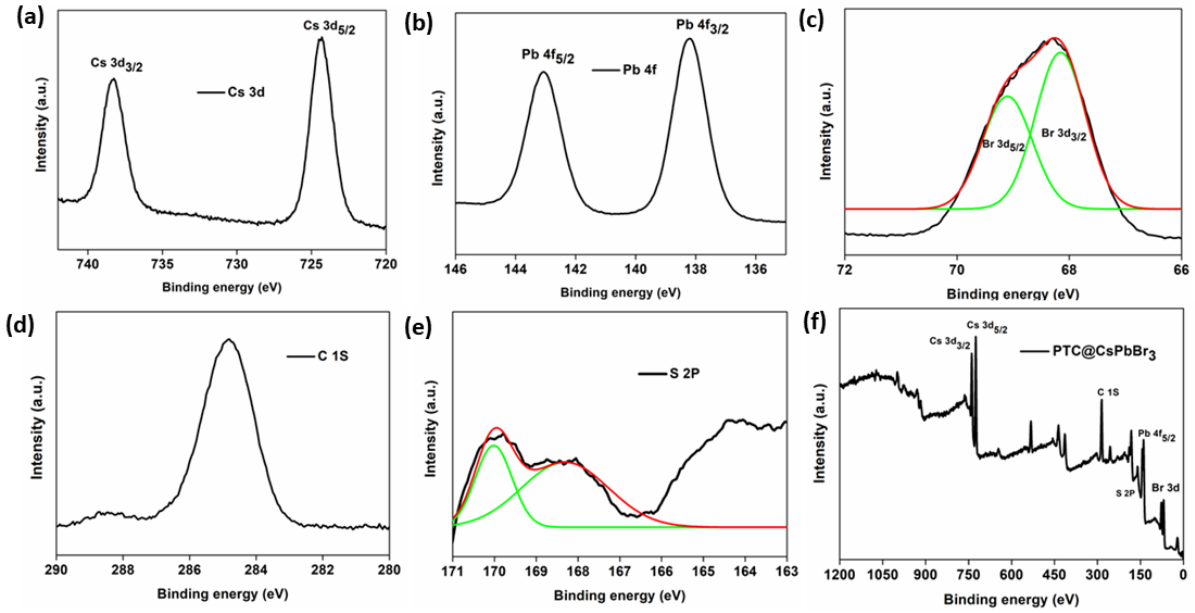

Figure 4.9 XPS survey of (a) Cs 3d spectrum, (b) Pb 4f spectrum, (c) Br 3d spectrum, (d) C 1s spectrum, (e) S 2p spectrum, and (f) prepared PTC@$CsPbBr_3$ spectrum

4.3.2 Morphological analysis

4.3.2.1 SEM analysis

The morphology of the perovskite crystals are shown *via* Scanning Electron Microscope (SEM) analysis (Figure 4.10). The synthesized *p*-thiocresol passivated $CsPbBr_3$ crystals was found in an orthorhombic-shaped morphology.

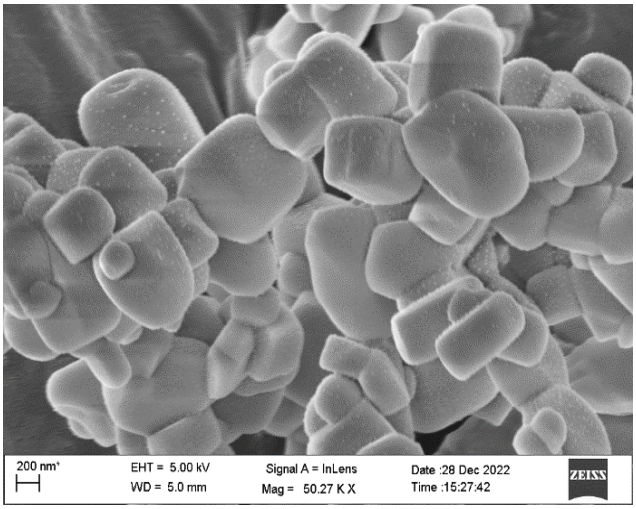

Figure 4.10 SEM image of *p*-thiocresol passivated $CsPbBr_3$

4.3.2.2 TEM analysis

The crystal structure was further confirmed by Transmission Electron Microscopy (TEM) analysis (Figure 4.11). The TEM image of PTC@$CsPbBr_3$ reveals of orthorhombic-shaped structure with an average particle size of 75.17 nm. The inset image showed the interplanar distance of 0.40 nm corresponding to the (110) plan of PTC@$CsPbBr_3$. Also, the selected area diffraction pattern (SAED) of the PNPs with an interplanar spacing of 0.40 nm also confirmed the (110) plane of synthesized perovskite (Figure 4.11b).

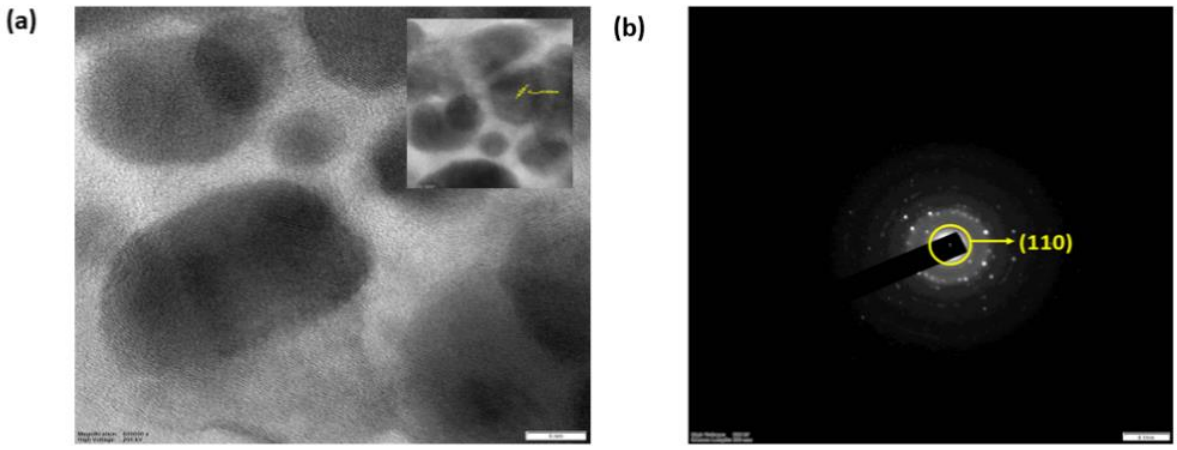

Figure 4.11 (a) TEM images of the PTC@$CsPbBr_3$ and inset image indexed with interplanar distance, and (b) Selected Area Diffraction (SAED) pattern of PTC@$CsPbBr_3$

4.3.3 Study of stability of PTC@$CsPbBr_3$

The stability of the PTC@$CsPbBr_3$ was tested under different conditions. The fluorescence intensity of PTC@$CsPbBr_3$ was recorded in different polar and non-polar solvents like water, ethanol, hexane, and toluene (Figure 4.12a). The luminescence

intensity was more in the case of toluene dispersion than in the other polar and non-polar solvents. Hence, toluene was chosen as a solvent to perform all our sensing experiments. Additionally, the stability test was confirmed by performing fluorescence measurements of PTC@$CsPbBr_3$ upto 60 min in toluene dispersion at different time intervals. The fluorescence intensity of the sensor probe does not noticeably change (Figure 4.12b). This study confirmed that the PTC layer were successfully protected $CsPbBr_3$ PNPs well.

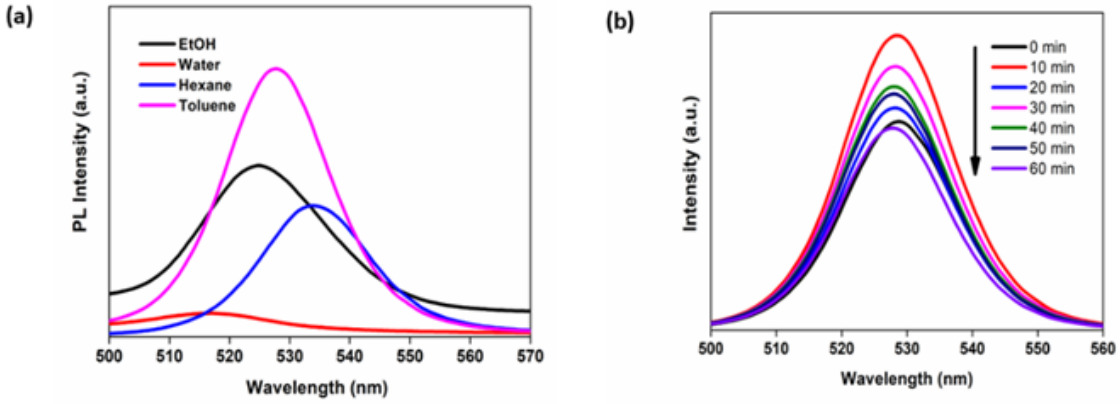

Figure 4.12 (a) Effects of different polar solvents on the fluorescence properties of PTC@$CsPbBr_3$, and (b) Stability of PTC@$CsPbBr_3$ in toluene

The stability of the designed sensor was studied under 80% humid conditions by recording fluorescence intensity at different time intervals for a period of 12 hours. Only 33.22% of degradation was found in the case of thiol-passivated perovskite nanocrystals (Figure 4.13a). However, the pristine perovskites showed higher degradation with a percentage degradation of 56.18%. To check the luminescence stability of PTC@$CsPbBr_3$ NPs against temperature, the temperature stability test was performed by recording the fluorescence intensity of the perovskite dispersion by increasing the temperature to 110 °C. The calculated percentage degradation of PTC@$CsPbBr_3$ was found to be 9.4% (Figure 4.13b) whereas, the value for pristine $CsPbBr_3$ was found as 42.73% (Figure 4.13c). Further the photostability test of the perovskite dispersion was investigated by illuminating the perovskite dispersion under a 365 nm UV-lamp for a period of 8 hours. The percentage degradation of PTC@$CsPbBr_3$ was 55.45%. However, the value for pristine $CsPbBr_3$ was found as 69.09%. To employ the water resistance test of the perovskite dispersion, aliquot 0.1 mL of water was added to a 3 mL perovskite. The respective fluorescence was measured with an excitation wavelength of 380 nm. The calculated percentage degradation of PTC@$CsPbBr_3$ is found as 63.27 %. However, the

value for $CsPbBr_3$ is 96.11%. From the above results, it can be concluded that *p*-thiocresol ligand successfully made halide perovskite more stable than pristine one against high humidity, increased temperature, and under UV-lamp irradiation.

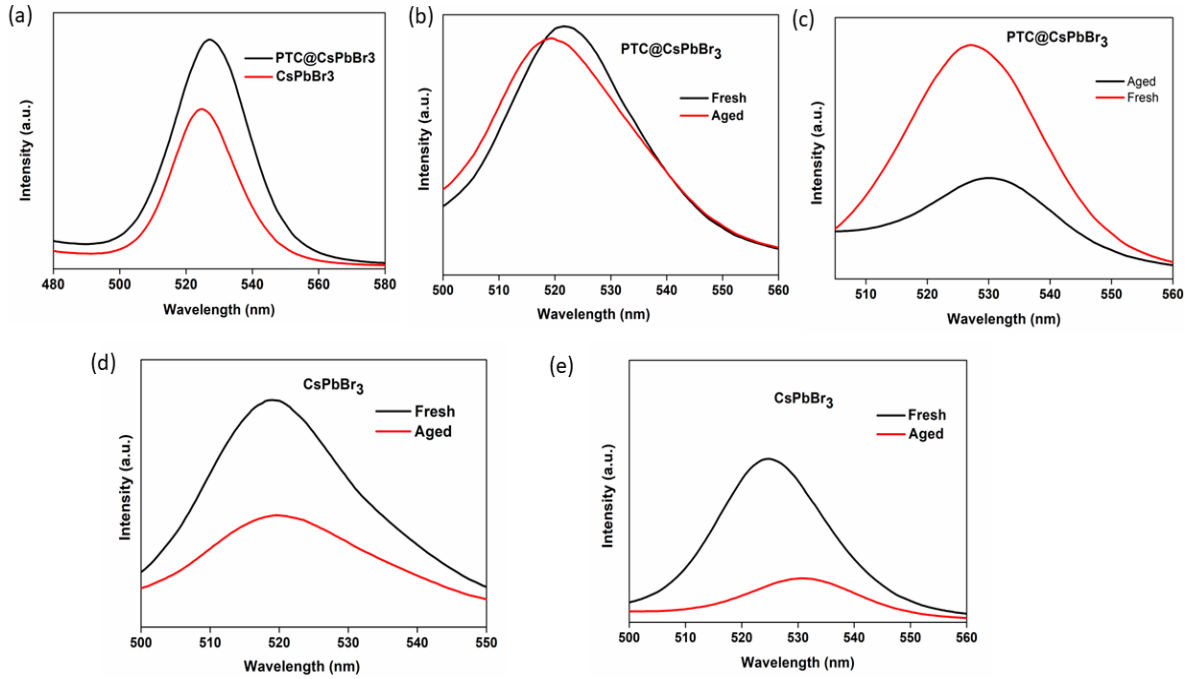

Figure 4.13 (a) Luminescence behaviour of PTC@$CsPbBr_3$ & $CsPbBr_3$ under 80% humid condition for a period of 12 hours, (b) Variation of luminescence intensity of PTC@$CsPbBr_3$ as a function of temperature up to 110 ℃, (c) UV photostability test of PTC@$CsPbBr_3$ under the irradiation of 365 nm UV lamp, (d) Variation of luminescence intensity of bare $CsPbBr_3$ as a function of temperature up to 110 ℃, (e) UV photostability test of bare $CsPbBr_3$

4.3.4 Sensitivity of $CsPbBr_3$ towards cholesterol

The high stability with excellent optoelectronic properties of PTC@$CsPbBr_3$ makes it to study as a fluorescence sensing probe for cholesterol. The sensing experiments were carried out in a perovskite dispersion in toluene (0.1 mmol of $CsPbBr_3$ into 10 mL toluene) with the addition of a different amount of analyte cholesterol. First, the fluorescence titration experiments were carried out in a suspension of $CsPbBr_3$ perovskite in toluene with a concentration of (0.57 g/100 mL). The dispersion was further sonicated for 30 min to get a homogeneous suspension. To an aliquot of 3 mL, various concentrations of cholesterol were added. The fluorescence measurements were carried out with an excitation wavelength of 380 nm. With the gradual addition of cholesterol solution (0.1 mmol/10 mL toluene), the luminescence intensity of PNPs gradually decreased (Figure 4.14a). The cholesterol was added with a concentration

ranging from 0.039 to 0.30 µM. The quenching efficiency was calculated using the following Stern-Volmer equation:

$$\frac{I_0}{I} = 1 + K_{sv}[C_{Cholesterol}]$$

In this equation, I_0 is the initial PL intensity of PTC@$CsPbBr_3$ without adding the analyte cholesterol, and I is the luminescence intensity of PTC@$CsPbBr_3$ with the addition of cholesterol. C is the added concentration of cholesterol and K_{sv} is the Stern Volmer constant of the analyte.

From the calculations, it was found that titration data was well fitted in the linear equation I_0/I= 9.35x+1.09 with a correlation efficiency of 0.96 (Figure 4.14b). The calculated detection limit (3σ/k) was found as 0.24 ppm, where k was the slope of the calibration graph and σ was the standard deviation for blank samples of repeat times n = 10. The Stern-Volmer constant K_{sv} for the titration against cholesterol was found as 9.36×10^6 M^{-1}. While comparing the detection limit with other fluorescence sensors (Table 4.2), it was found that our designed sensor can able to detect cholesterol with lower detection limit.

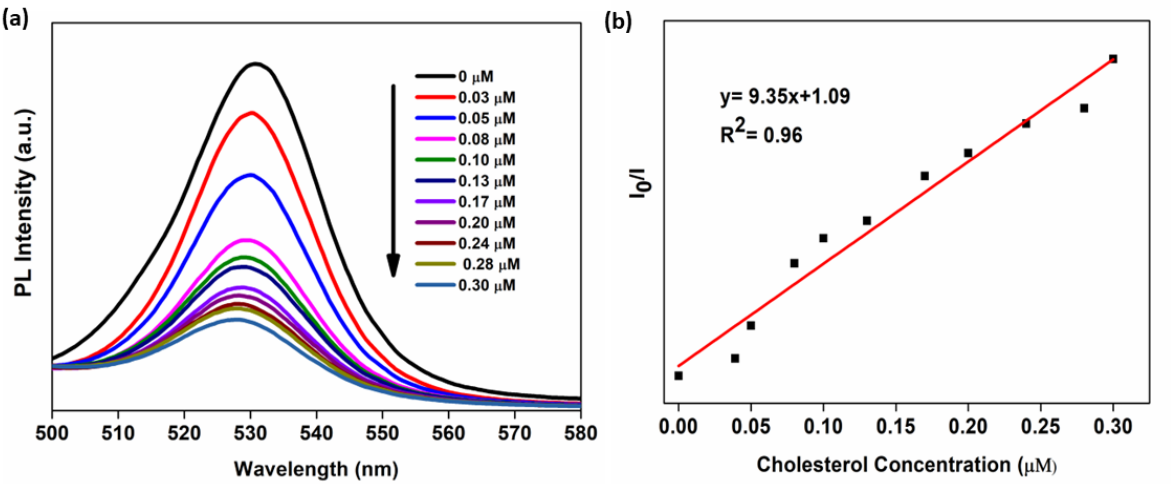

Figure 4.14 (a) Photoluminescence spectra of PTC@$CsPbBr_3$ with the addition of different concentrations of cholesterol, and (b) the Stern-Volmer plot of the sensor probe against different concentrations of cholesterol

The response time of the designed fluorescence system was further evaluated with the addition of 0.13 µM cholesterol to the 3 mL perovskite dispersion. From the

figure 4.15a, it was observed that after 10s the fluorescence intensity became stable. Thus, the response time of the sensor toward the analyte was 10s. At different pH conditions, the quenching abilities of the sensor probe PTC@$CsPbBr_3$ were evaluated (Figure 4.15b). In this case, it was noticed that the probe was failed to perform in the acidic pH. In acidic pH, there might be structural distortion between the bromide ion from the perovskite surface with the proton present in the medium. However, when the pH of the medium was increased from neutral to basic consecutively; the quenching behaviour of the probe increased and delivered better performance.

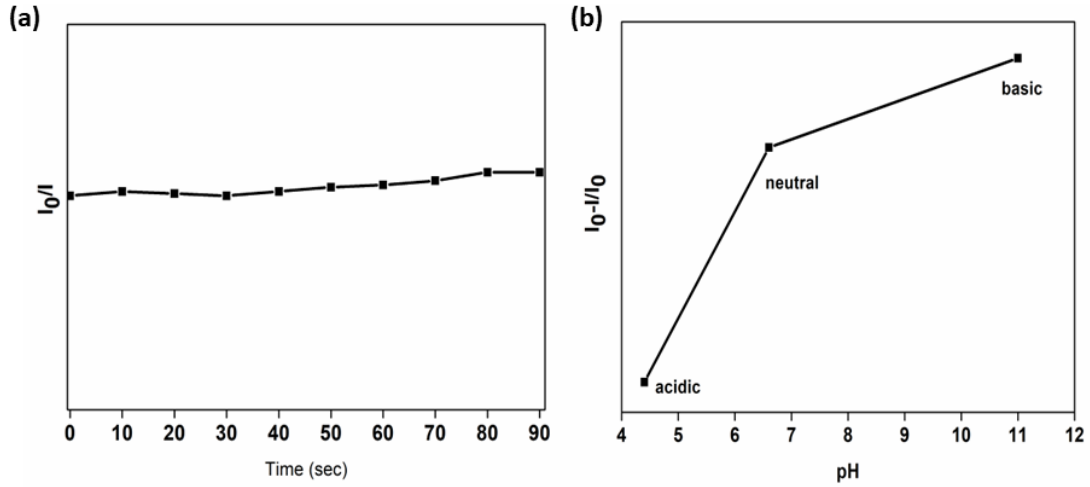

Figure 4.15 (a) Fluorescence intensity of PTC@$CsPbBr_3$ after adding 0.30 μM cholesterol at different response times, and (b) effect of different pH on the PL quenching of PTC@$CsPbBr_3$ towards cholesterol detection

Table 4.2 A Comparative study of a few fluorescence sensor probe systems for detection of cholesterol

Entry	Sensor probe	LOD(μM)	ref
1	Cholesterol oxidase-functionalized mesoporous silica nanoparticle@ZIF-8 core-shell nanocomposites.	0.89 nM	40
2	Nitrogen, cobalt co-doped carbon dots (N, Co-CDs) with 2,3-diaminophenazine (DAP)	3.4 nM	41
3	Carboxymethyl β-cyclodextrin (β-CMCD) was grafted onto the luminescent metal organic framework	0.4μM	42

4	Nitrogen-doped graphene quantum dots	0.4 μM	43
5	Au@CD	0.0024 mM	44
6	Enzyme-modified CdSe/ZnS	0.01 mM	45
7	CuINS/ZnS	0.222 mM	46
8	Gold Carbon dot	10 nM	47
9	Au NPs–β-CD	9 nM	48
10	CeO_2-CD	0.35μM	49
11	N doped Carbon quantum dot/ MnO2 nanowire	0.004 μM	50
12	CIS@ZnS QDs	10 nM	51
13	β-CD-RhB	3 μM	52
14	DNA-stabilized silver nanoclusters with guanine	0.15 μM	53
15	Poly(vinyl pyrrolidone)-protected gold nanoparticles (PVP-AuNPs) and fluorescent BSA-protected gold nanoclusters (BSA-AuNCs)	0.8 μM	54
16	Carbon nanodot	3.64 μM	55
17	Pd Nanoclusters Confined in ZIF-8	0.092 μM	56

4.3.5 Selective sensing of PTC@$CsPbBr_3$ towards cholesterol

Furthermore, the selectivity of the sensing probe PTC@$CsPbBr_3$ was evaluated with respect to some potential biologically important interfering compounds such as glycine, urea, ascorbic acid, fructose, *L*-Cystine, uracil, adenine, and sodium chloride (NaCl). All the experiments were carried out under the same reaction condition. The selectivity experiments reveals that the counterparts have negligible influence on the sensor probe which verifies that the PTC@$CsPbBr_3$ sensor have a high selectivity towards cholesterol detection (Figure 4.16).

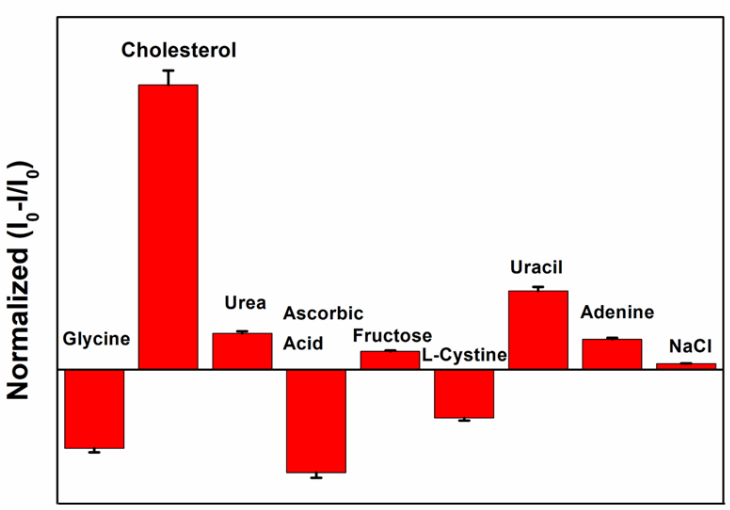

Figure 4.16 Selectivity research of PTC@CsPbBr$_3$ towards cholesterol (0.30 μM) under different biologically relevant interfering molecules and metal ions (0.30 μM)

4.3.6 Sensing mechanism of PTC@CsPbBr$_3$ towards cholesterol

Figure 4.17a shows that there was no spectral overlap between the absorption spectra of the analyte cholesterol and luminescence spectra of the PTC@CsPbBr$_3$ (Figure 4.17a). From which, it can be understood that the probability mechanism of the quenching is through foster resonant energy transfer (FRET) is low [57]. There is no significant shift of the emission peak of PTC@CsPbBr$_3$, when cholesterol was added; which eliminates the probability of the intermolecular charge transfer (ICT) mechanism [58]. XRD analysis revealed the presence of the characteristic signal even after the exposure to cholesterol (Figure 4.17b). This indicates, the analyte (cholesterol) does not make any structural changes in the perovskite lattice structure [38]. The same conclusion was also confirmed from the FE-SEM image of recovered PTC@CsPbBr$_3$ (Figure 4.18a). Comparison of the FT-IR spectra of PTC@CsPbBr$_3$ and recovered PTC@CsPbBr$_3$ confirmed that there were not any distinguishable changes (Figure 4.18b), and this concludes that exciplex/excimer formation is less during the detection process [59]. From elemental mapping images it was confirmed that the elements Cs, Pb, Br, C, O, and S homogeneously distributed in the perovskite crystal structure which reveals that cholesterol uniformly reacts with PTC@CsPbBr$_3$ (Figure 4.19).

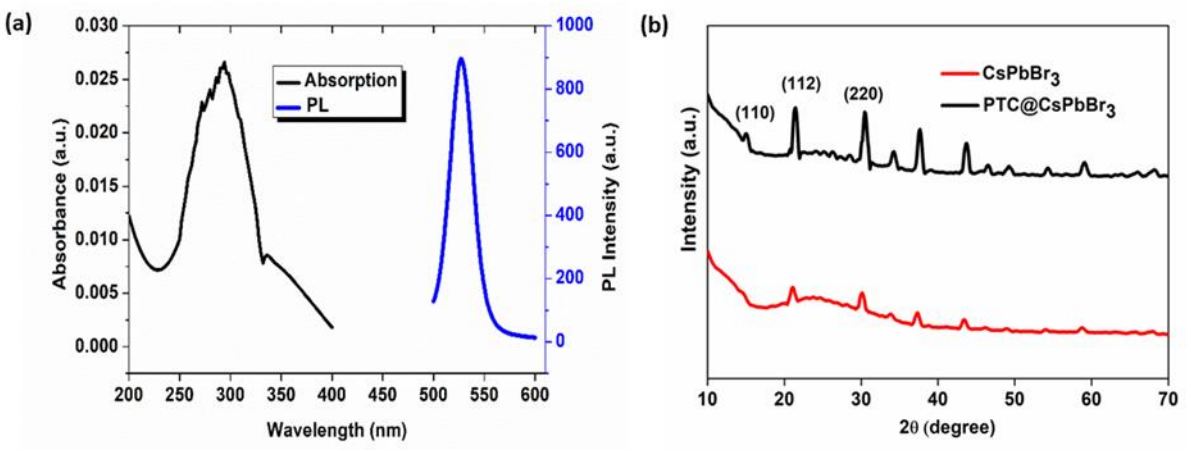

Figure 4.17 (a) UV-Vis absorption spectra of cholesterol and Luminescence spectra of PTC@CsPbBr3, and (b) P-XRD spectra of PTC@CsPbBr3 and pristine CsPbBr3

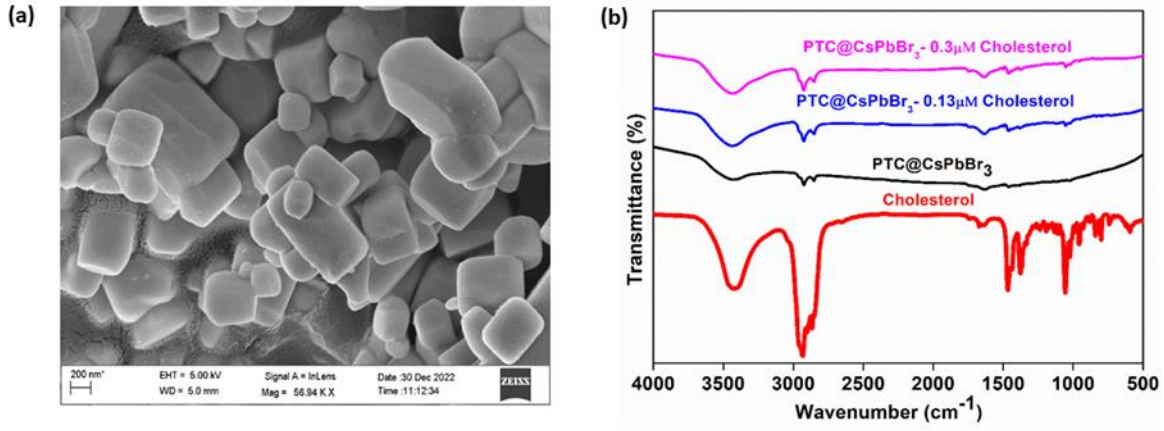

Figure 4.18 (a) FE-SEM image of recovered PTC@CsPbBr3, and (b) FT-IR spectra of PTC@CsPbBr3 in the absence/presence of 0.13 μM cholesterol & 0.3 μM cholesterol

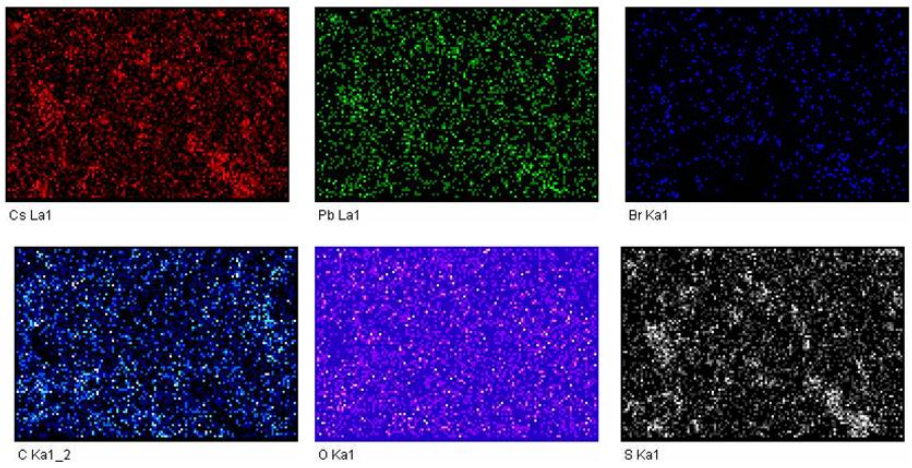

Figure 4.19 Elemental image of PTC@CsPbBr3 cholesterol

The mechanism of the detection process was further validated with the time-resolved photoluminescence spectra (TRPL) analysis (Figure 4.20). The excitation wavelength in this analysis was 380 nm. The bi-exponential decay graphs concluded that the calculated average lifetime of PTC@$CsPbBr_3$ was 5.91 ns, while the value declined to 1.4 ns in presence of 0.13 µM cholesterol. The shortened lifetime of the sensor probe PTC@$CsPbBr_3$ in presence of cholesterol indicates that the detection of cholesterol is gone through the dynamic quenching mechanism. With the gradual addition of the analyte cholesterol on the perovskite dispersion most likely creates some H-bonding interaction between the thiol group of PTC@$CsPbBr_3$ PNPs with the hydroxyl group of cholesterol and later, this interaction triggers some non-radioactive decay [60,61]. The interaction between Pb^{2+} from $CsPbBr_3$ with the O atom of cholesterol also might cause some cationic vacancies. Similarly, interactions between the Br^- ion with the H-atom of cholesterol form anionic vacancies. Due to these interactions, some charge recombination takes place in the perovskite crystal with the addition of analyte cholesterol and results in some quenching of the emission peak at 530 nm. The mechanism was further verified with the temperature study. With an increase in temperature from 286K to 303 K, the Stern-Volmer constant was increased from 8.25 $\times 10^6$ M^{-1} to 16.26 $\times 10^6$ M^{-1} (Figure 4.21) and confirmed the detection of cholesterol by PTC@$CsPbBr_3$ proceeded dynamic quenching mechanism [59]. The intensity of solid-state absorbance spectra of the sensor probe PTC@$CsPbBr_3$ decreases upon exposure with 0.30 µM cholesterol and proved the applicability of the designed senor in the solid-state detection process (Figure 4.22).

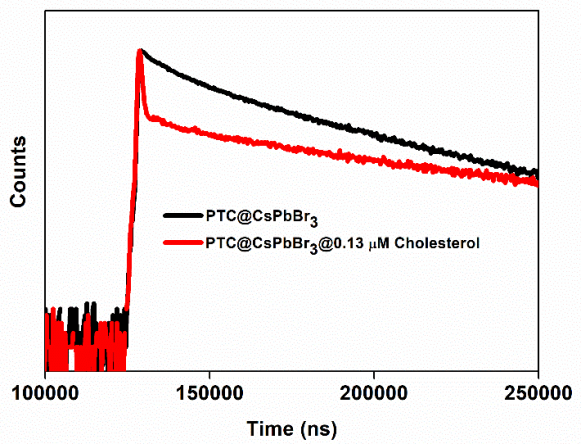

Figure 4.20 TRPL spectra of PTC@$CsPbBr_3$ in the absence/presence of 0.13 µM cholesterol

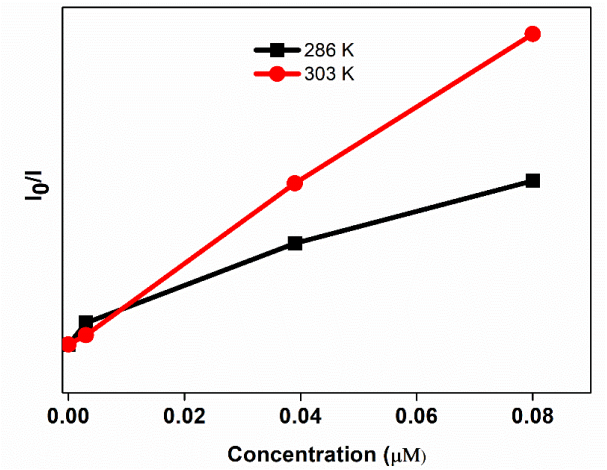

Figure 4.21 Stern- Volmer plot of PTC@$CsPbBr_3$ in the presence of cholesterol at 286 K & 303K

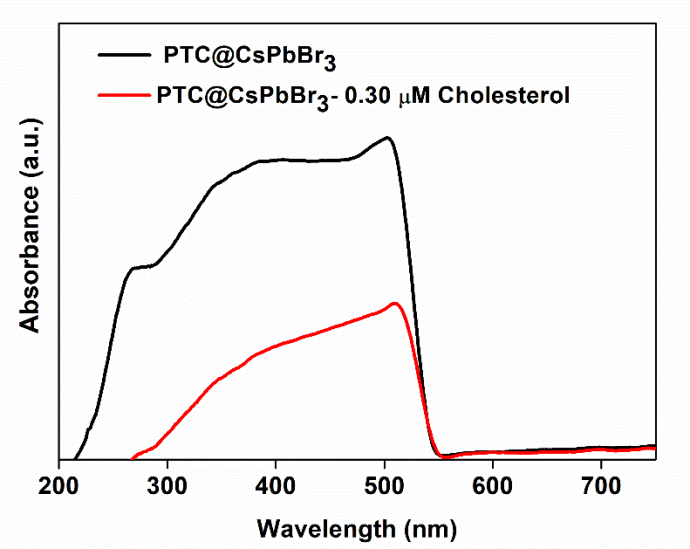

Figure 4.22 Solid-state UV-Vis absorption of PTC@ $CsPbBr_3$ titrated with 0.30 μM concentrations of cholesterol

4.3.7 Detection of cholesterol in an aqueous environment

The potential applicability of the designed sensor of PTC@$CsPbBr_3$ in humid conditions was further examined by dispersing cholesterol in an aqueous solution. In this study, it is seen that the luminescence intensity of the PTC@$CsPbBr_3$(0.1mmol/10mL) gradually decreased after the addition of cholesterol (0.1 mmol/10 mL) (Figure 4.23).

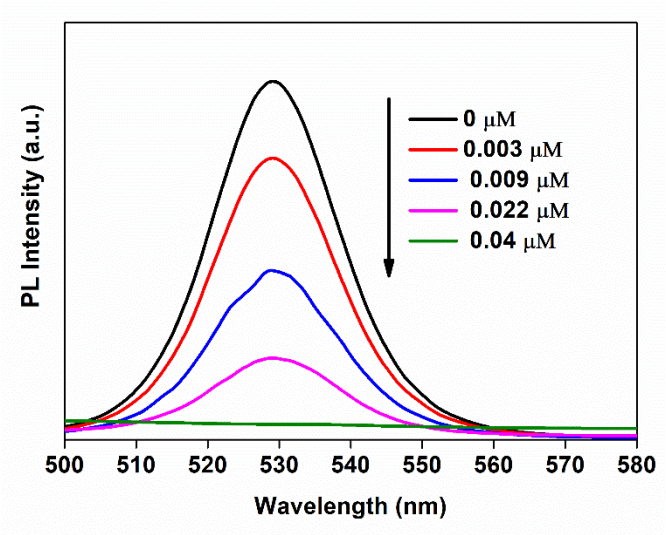

Figure 4.23 PL quenching of PTC@$CsPbBr_3$ (0.1 mmol) in presence of various cholesterol concentrations (0.1 mmol) dispersed in water

4.3.8 Control Experiment in Water

The pertinency of the sensor probe PTC@$CsPbBr_3$ in the aqueous environment was checked in this study. For the analysis, 3mL of perovskite solution (0.1 mmol in 10 mL toluene) was taken as a stock solution and the analyte cholesterol (0.1 mmol) was dispersed in 10 mL water. Then, a dispersion solution was prepared by mixing 1 mL of the above cholesterol solution with 2 mL toluene in a volume ratio of (1:2). In this analysis, we found that the luminescence peak of PTC@ $CsPbBr_3$ gradually quenched with the addition of cholesterol solution in the prepared biphasic mixture (Figure 4.24). The emission peak of PTC@$CsPbBr_3$ in toluene showed gradual increase with the addition of H_2O and toluene solution in the same volume ratio without cholesterol. This difference luminescence behaviour of the PTC@$CsPbBr_3$ makes it effective as the addition of an optimum volume of water in the reaction medium. In these quenching experiments, it was confirmed that the solvent did not interfere with the quenching due to the analyte. The distinguished emission behaviour conclusively justified the applicability of the designed sensor PTC@$CsPbBr_3$ towards cholesterol detection in an aqueous environment.

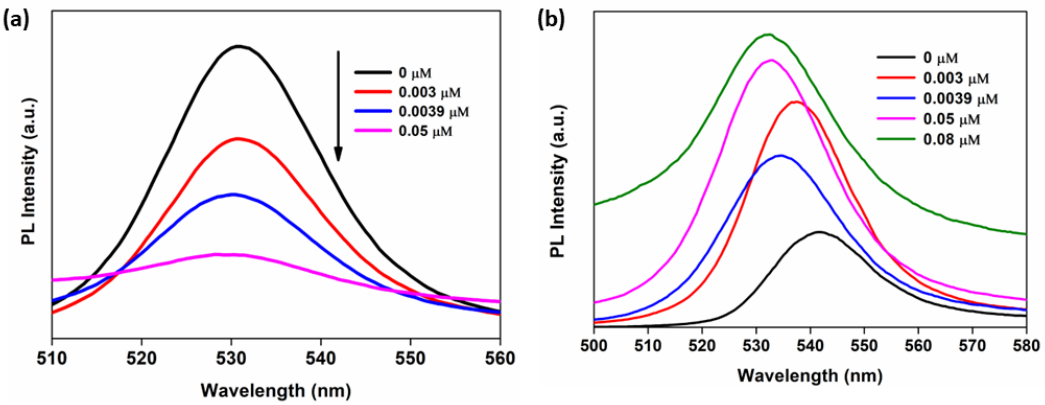

Figure 4.24 Validation of the designed sensor (a) with the gradual addition of cholesterol, (b) upon the addition of different volumes of water

4.4 Determination of cholesterol in human blood serum

The practical utility of the designed sensor was investigated by the quantitative determination of cholesterol in the real sample (human blood serum). To determine the appropriate concentration of cholesterol in the human blood, samples were diluted with distilled water with 100-fold dilution. Various concentrations of cholesterol are added in the diluted serum samples. As shown in the Table 4.3, the obtained results are shown with recoveries of 92%, 102.56%, and 107.6%. This analysis demonstrates the potential applicability of the sensor probe for detecting cholesterol in real samples.

Table 4.3 Determination of cholesterol in human-blood samples using PTC@$CsPbBr_3$

Dilution	Added cholesterol (μM)	Found cholesterol (μM)	Recovery (%)	RSD (%)
100-fold	0.050	0.046	92	0.57
	0.039	0.040	102.56	1.81
	0.13	0.14	107.6	1

4.5 Conclusion

In summary, this chapter mentioned the development of another sensing system where *p*-thiocresol as a passivating ligand for the controlled synthesis of $CsPbBr_3$ perovskite nanoparticles at room temperature. The synthesized PTC@$CsPbBr_3$ perovskites were stable in high temperature and high humidity conditions. The work demonstrated PTC@$CsPbBr_3$ as an optical sensor for detecting cholesterol with high selectivity and sensitivity. The mechanism of the quenching process was found as the dynamic

quenching mechanism. The proposed sensor can be able to detect cholesterol in the range of 0.0039-0.030 μM with an ultra-low detection limit of 0.24 ppm with the fast response time of 10 s. The efficacy of the sensor was further examined by applying it to the detection of cholesterol in human blood serum. Due to the high recovery percentage, it can be expected that the designed sensor has potential applications in biomedical fields to detect cholesterol related problems in human health.

4.6 Bibliography

[1] Priyadarshini, E. and Rawat, K. Au@carbon-dot nanoconjugates as a dual mode enzyme-free sensing platform for cholesterol. *Journal of Materials Chemistry B*, 5(27):5425-5432, 2017.

[2] Soylemez, S., Hacioglu, S. O., Kesik, M., Unay, H., Cirpan, A., and Toppare, L. A novel and effective surface design: conducting polymer/β-cyclodextrin host–guest system for cholesterol biosensor. *ACS Applied Materials & Interfaces*, 6(20):18290-18300, 2014.

[3] Zhang, X., Wei, M., L, B., Liu, Y., Liu, X., and Wei, W. Sensitive colorimetric detection of glucose and cholesterol by using Au@Ag-core–shell nanoparticles. *RSC Advances*, 6(41):35001-35007, 2016.

[4] Martin, S., Lamb, D., Lynch, J., and Reddy, S. Enzyme-based determination of cholesterol using the quartz crystal acoustic wave sensor. *Analytica Chimica Acta*, 487(1):91-100, 2003.

[5] Gupta, P., Rahaman, F., Gautam, P., Mondal, S., and Lekshmi, I. A non-enzymatic fluorometric detection of cholesterol *via* micelle induced supramolecular assembly using thiazole derived molecule. *Journal of Photochemistry and Photobiology A: Chemistry*, 421:113527, 2021.

[6] Amiri, M. and Arshi, S. An overview on electrochemical determination of cholesterol. *Electroanalysis*, 32(7):1391-1407, 2020.

[7] Carlson, S. E. and Goldfarb, S. A sensitive enzymatic method for the determination of free and esterified tissue cholesterol. *Clinica Chimica Acta*, 79(3):575-582, 1977.

[8] Albuquerque, T. G., Oliveira, M. B. P., Sanches-Silva, A., and Costa, H. S. Cholesterol determination in foods: Comparison between high performance and ultra-high performance liquid chromatography. *Food Chemistry*, 193:18-25, 2016.

[9] Wolfbeis, O. S. Materials for fluorescence-based optical chemical sensors. *Journal of Materials Chemistry*, 15(27-28):2657-2669, 2005.

[10] Che, Y., Yang, X., Loser, S., and Zang, L. Expedient vapor probing of organic amines using fluorescent nanofibers fabricated from an n-type organic semiconductor. *Nano Letters*, 8(8):2219-2223, 2008.

[11] Scanlan, K., Kanibolotsky, A. L., Breig, B., Hedley, G. J., and Skabara, P. J. Tetrathiafulvalene–oligofluorene star-shaped systems: new semiconductor materials for fluorescent moisture indicators. *Journal of Materials Chemistry C*, 7(22):6582-6591, 2019.

[12] Liu, J., Li, R., and Yang, B. Carbon dots: A new type of carbon-based nanomaterial with wide applications. *ACS Central Science*, 6(12):2179-2195, 2020.

[13] Khan, Z. G. and Patil, P. O. A comprehensive review on carbon dots and graphene quantum dots based fluorescent sensor for bio-thiols. *Microchemical Journal*, 157:105011, 2020.

[14] Cayuela, A., Soriano, M., Carrillo-Carrión, C., and Valcárcel, M. Semiconductor and carbon-based fluorescent nanodots: the need for consistency. *Chemical Communications*, 52(7):311-1326, 2016.

[15] Kulbak, M., Gupta, S., Kedem, N., Levine, I., Bendikov, T., Hodes, G., and Cahen, D. Cesium enhances long-term stability of lead bromide perovskite-based solar cells. *The Journal of Physical Chemistry Letters*, 7(1):167-172, 2016.

[16] Wan, X., Yu, Z., Tian, W., Huang, F., Jin, S., Yang, X., Cheng, Y. B., Hagfeldt, A., and Sun, L. Efficient and stable planar all-inorganic perovskite solar cells based on high-quality $CsPbBr_3$ films with controllable morphology. *Journal of Energy Chemistry*, 46:8-15, 2020.

[17] Wang, T., Wei, X., Zong, Y., Zhang, S., and Guan, W. An efficient and stable fluorescent sensor based on APTES-functionalized $CsPbBr_3$ perovskite quantum dots for ultrasensitive tetracycline detection in ethanol. *Journal of Materials Chemistry C*, 8(35):12196-12203, 2020.

[18] Li, Z. J., Hofman, E., Li, J., Davis, A. H., Tung, C. H., Wu, L. Z., and Zheng, W. Photoelectrochemically active and environmentally stable $CsPbBr_3/TiO_2$ core/shell nanocrystals. *Advanced Functional Materials*, 28(1):1704288, 2018.

[19] Luo, S. and Daoud, W. A. Recent progress in organic–inorganic halide perovskite solar cells: mechanisms and material design. *Journal of Materials Chemistry A*, 3(17):8992-9010, 2015.

[20] Ahmadi, M., Wu, T., and Hu, B. A review on organic–inorganic halide perovskite photodetectors: device engineering and fundamental physics. *Advanced Materials*, 29(41):1605242, 2017.

[21] Misra, R. K., Cohen, B. E., Iagher, L., and Etgar, L. Low-dimensional organic–inorganic halide perovskite: structure, properties, and applications. *ChemSusChem*, 10(19):3712-3721, 2017.

[22] Liu, P., Chen, W., Wang, W., Xu, B., Wu, D., Hao, J., Cao, W., Fang, F., Li, Y., and Zeng, Y. Halide-rich synthesized cesium lead bromide perovskite nanocrystals for light-emitting diodes with improved performance. *Chemistry of Materials*, 29(12):5168-5173, 2017.

[23] Zhou, Y., Gu, Q., Li, Y., Tao, L., Tan, H., Yin, K., Zhou, J., and Guo, S. Cesium Lead Bromide Perovskite-Based Lithium–Oxygen Batteries. *Nano letters*, 21(11):4861-4867, 2021.

[24] Hu, Y., Wang, Q., Shi, Y. L., Li, M., Zhang, L., Wang, Z. K., and Liao, L. S. Vacuum-evaporated all-inorganic cesium lead bromine perovskites for high-performance light-emitting diodes. *Journal of Materials Chemistry C*, 5(32):8144-8149, 2017.

[25] Sutton, R. J., Eperon, G. E., Miranda, L., Parrott, E. S., Kamino, B. A., Patel, J. B., Hörantner, M. T., Johnston, M. B., Haghighirad, A. A., and Moore, D. T. Bandgap-tunable cesium lead halide perovskites with high thermal stability for efficient solar cells. *Advanced Energy Materials*, 6(8):1502458, 2016.

[26] Tong, G., Chen, T., Li, H., Qiu, L., Liu, Z., Dang, Y., Song, W., Ono, L. K., Jiang, Y., and Qi, Y. Phase transition induced recrystallization and low surface potential barrier leading to 10.91% efficient $CsPbBr_3$ perovskite solar cells. *Nano Energy*, 65:104015, 2019.

[27] Sanjayan, C., Jyothi, M., and Balakrishna, R. G. Stabilization of $CsPbBr_3$ quantum dots for photocatalysis, imaging and optical sensing in water and biological medium: a review. *Journal of Materials Chemistry C*, 10(18):6935-6956, 2022.

[28] Shankar, H., Yu, W. W., Kang, Y., and Kar, P. Significant boost of the stability and PLQY of $CsPbBr_3$ NCs by Cu-BTC MOF. *Scientific Reports*, 12(1):7848, 2022.

[29] Wu, Y., Wei, C., Li, X., Li, Y., Qiu, S., Shen, W., Cai, B., Sun, Z., Yang, D., and Deng, Z. In situ passivation of $PbBr_6^{4-}$ octahedra toward blue luminescent $CsPbBr_3$ nanoplatelets with near 100% absolute quantum yield. *ACS Energy Letters*, 3(9):2030-2037, 2018.

[30] Ji, Y., Wang, M., Yang, Z., Qiu, H., Padhiar, M. A., Zhou, Y., Wang, H., Dang, J., Gaponenko, N. V., and Bhatti, A. S. Trioctylphosphine-assisted pre-protection low-temperature solvothermal synthesis of highly stable $CsPbBr_3/TiO_2$ nanocomposites. *The Journal of Physical Chemistry Letters*, 12(15):3786-3794, 2021.

[31] Shu, Y., Sun, L., Wang, Y., Jin, D., Xu, Q., and Hu, X. Polymer surface ligand and silica coating induced highly stable perovskite nanocrystals with enhanced aqueous fluorescence for efficient Hg^{2+} and glutathione detection. *Analyst*, 146(22):6798-6807, 2021.

[32] Xue, W., Zhong, J., Wu, H., Zhang, J., and Chi, Y. A visualized ratiometric fluorescence sensing system for copper ions based on gold nanoclusters/perovskite quantum dot@ SiO_2 nanocomposites. *Analyst*, 146(24):7545-7553, 2021.

[33] Huynh, K. A., Bae, S. R., Nguyen, T. V., Do, H. H., Heo, D. Y., Park, J., Lee, T. W., Le, Q. V., Ahn, S. H., and Kim, S. Y. Ligand-assisted sulfide surface treatment of $CsPbI_3$ perovskite quantum dots to increase photoluminescence and recovery. *ACS Photonics*, 8(7):1979-1987, 2021.

[34] Liji Sobhana, S., Vimala Devi, M., Sastry, T., and Mandal, A. B. CdS quantum dots for measurement of the size-dependent optical properties of thiol capping. *Journal of Nanoparticle Research*, 13:1747-1757, 2011.

[35] Ou, M., Tu, W., Yin, S., Xing, W., Wu, S., Wang, H., Wan, S., Zhong, Q., and Xu, R. Amino-assisted anchoring of $CsPbBr_3$ perovskite quantum dots on porous *g*-C_3N_4 for enhanced photocatalytic CO_2 reduction. *Angewandte Chemie International Edition*, 130(41):13758-13762, 2018.

[36] Ouhaddouch, H., Cheikh, A., Idrissi, M., Draoui, M., and Bouatia, M. FT-IR spectroscopy applied for identification of a mineral drug substance in drug products: Application to bentonite. *Journal of Spectroscopy*, 2019.

[37] Allen, G. and Colclough, R. 777. Hydrogen bonding of the thiol group in phosphinodithioic acids. *Journal of the Chemical Society,* :3912-3915, 1957.

[38] Qu, S., Li, Z., and Jia, Q. Detection of purine metabolite uric acid with picolinic-acid-functionalized metal–organic frameworks. *ACS Applied Materials & Interfaces*, 11(37):34196-34202, 2019.

[39] Siril, P., Shiju, N., Brown, D., and Wilson, K. Optimizing catalytic properties of supported sulfonic acid catalysts. *Applied Catalysis A: General*, 364(1-2):95-100, 2009.

[40] Wang, K., Ren, H., Li, N., Tan, X., and Dang, F. Ratio-metric fluorescence sensor based on cholesterol oxidase-functionalized mesoporous silica nanoparticle@ZIF-8 core-shell nanocomposites for detection of cholesterol. *Talanta*, 188:708-713, 2018.

[41] Huang, S., Yang, E., Yao, J., Chu, X., Liu, Y., Zhang, Y., and Xiao, Q. Nitrogen, cobalt co-doped fluorescent magnetic carbon dots as ratiometric fluorescent probes for cholesterol and uric acid in human blood serum. *ACS Omega*, 4(5):9333-9342, 2019.

[42] Gong, M., Yang, J., Li, Y., Zhuang, Q., and Gu, J. Substitution-type luminescent MOF sensor with built-in capturer for selective cholesterol detection in blood serum. *Journal of Materials Chemistry C*, 7(40):12674-12681, 2019.

[43] Sun, L., Li, S., Ding, W., Yao, Y., Yang, X., and Yao, C. Fluorescence detection of cholesterol using a nitrogen-doped graphene quantum dot/chromium picolinate complex-based sensor. *Journal of Materials Chemistry B*, 5(45):9006-9014, 2017.

[44] Sun, J., Wang, S., and Gao, F. Covalent surface functionalization of semiconducting polymer dots with β-cyclodextrin for fluorescent ratiometric assay of cholesterol through host–guest inclusion and FRET. *Langmuir*, 32(48):12725-12731, 2016.

[45] Kim, K. E., Kim, T. G., and Sung, Y. M. Fluorescent cholesterol sensing using enzyme-modified CdSe/ZnS quantum dots. *Journal of Nanoparticle Research*, 14:1-9, 2012.

[46] Adel, R., Ebrahim, S., Shokry, A., Soliman, M., and Khalil, M. Nanocomposite of CuInS/ZnS and nitrogen-doped graphene quantum dots for cholesterol sensing. *ACS Omega*, 6(3):2167-2176, 2021.

[47] Barua, S., Gogoi, S., and Khan, R. Fluorescence biosensor based on gold-carbon dot probe for efficient detection of cholesterol. *Synthetic Metals*, 244:92-98, 2018.

[48] Abdolmohammad-Zadeh, H. and Ahmadian, F. A fluorescent biosensor based on graphene quantum dots/zirconium-based metal-organic framework

nanocomposite as a peroxidase mimic for cholesterol monitoring in human serum. *Microchemical Journal*, 164:106001, 2021.

[49] Zhang, N., Liu, Y., Tong, L., Xu, K., Zhuo, L., and Tang, B. A novel assembly of Au NPs–β-CDs–FL for the fluorescent probing of cholesterol and its application in blood serum. *Analyst*, 133(9):1176-1181, 2008.

[50] Dewangan, L., Korram, J., Karbhal, I., Nagwanshi, R., and Satnami, M. L. N-doped carbon quantum dot-MnO_2 nanowire fret pairs: detection of cholesterol, glutathione, acetylcholinesterase, and chlorpyrifos. *ACS Applied Nano Materials*, 4(12):13612-13624, 2021.

[51] Mir, I. A., Kumar, S., Bhat, M. A., Yuelin, X., Wani, A. A., and Zhu, L. Core@ shell quantum dots as a fluorescent probe for the detection of cholesterol and heavy metal ions in aqueous media. *Colloids and Surfaces A: Physicochemical and Engineering Aspects*, 626:127090, 2021.

[52] Ding, Y., Zhu, H., Zhang, X., Gao, J., Abdel-Halim, E., Jiang, L., and Zhu, J. J. An up-conversion nanocomposite for fluorescence resonance energy transfer-based cholesterol-sensing in human serum. *Nanoscale*, 6(24):14792-14798, 2014.

[53] Duan, M., Peng, Y., Zhang, L., Wang, X., Ge, J., Jiang, J., and Yu, R. DNA-stabilized silver nanoclusters with guanine-enhanced fluorescence as a novel indicator for enzymatic detection of cholesterol. *Analytical Methods*, 5(9):2182-2187, 2013.

[54] Chang, H. C., and Ho, J. A. A. Gold nanocluster-assisted fluorescent detection for hydrogen peroxide and cholesterol based on the inner filter effect of gold nanoparticles. *Analytical Chemistry*, 87(20):10362-10367, 2015.

[55] Gogoi, N., Agarwal, D. S., Sehgal, A., Chowdhury, D., and Sakhuja, R. One-pot synthesis of carbon nanodots in an organic medium with aggregation-induced emission enhancement (AIEE): a rationale for "enzyme-free" detection of cholesterol. *ACS Omega*, 2(7):3816-3827, 2017.

[56] Li, Y., Li, S., Bao, M., Zhang, L., Carraro, C., Maboudian, R., Liu, A., Wei, W., Zhang, Y., and Liu, S. Pd nanoclusters confined in ZIF-8 matrixes for fluorescent detection of glucose and cholesterol. *ACS Applied Nano Materials*, 4(9):9132-9142, 2021.

[57] He, L., Lin, W., Xu, Q., and Wei, H. A new strategy to construct a FRET platform for ratiometric sensing of hydrogen sulfide. *Chemical Communications*, 51(8):1510-1513, 2015.

[58] Vora, M., Kongor, A., Panchal, M., Athar, M., Verma, A., Panjwani, F., Jha, P., and Jain, V. A highly selective anthraquinone appended oxacalixarene receptor for fluorescent ICT sensing of F^- ions: an experimental and computational study. *Journal of Chemical Sciences*, 132:1-10, 2020.

[59] Jalili, R. and Khataee, A. Aluminum (III) triggered aggregation-induced emission of glutathione-capped copper nanoclusters as a fluorescent probe for creatinine. *Microchimica Acta*, 186:1-9, 2019.

[60] Kim, S. H., Kirakosyan, A., Choi, J., and Kim, J. H. Spectroscopic study on the interaction of organic-inorganic hybrid perovskite nanoparticles with linear aliphatic alcohols. *Dyes and Pigments*, 143:71-75, 2017.

[61] Huang, S., Guo, M., Tan, J., Geng, Y., Wu, J., Tang, Y., Su, C., Lin, C. C., and Liang, Y. Novel fluorescence sensor based on all-inorganic perovskite quantum dots coated with molecularly imprinted polymers for highly selective and sensitive detection of omethoate. *ACS Applied Materials & Interfaces*, 10(45):39056-39063, 2018.